Check for updates

View Article Online
View Journal

Nanoscale

Accepted Manuscript

This article can be cited before page numbers have been issued, to do this please use: D.W. Li, Q.M. Zou, H. Rabiee-Golgir, K. Keramatnejad , X. Huang, J. Song, Z. Xiao, L. Fan, X. Hong, L. Jiang, J. silvain, S. Sun and Y. Lu, *Nanoscale*, 2017, DOI: 10.1039/C7NR01712J.

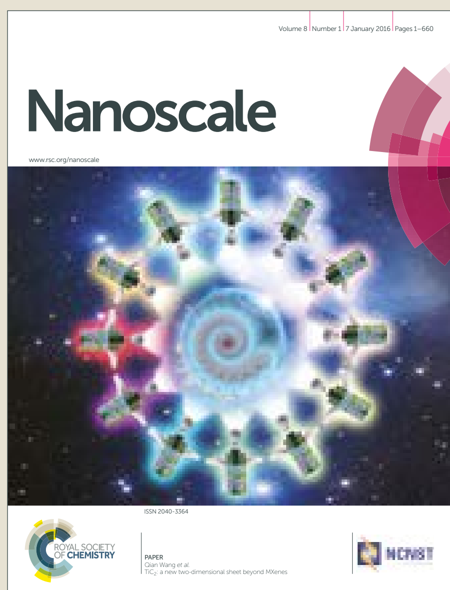

This is an Accepted Manuscript, which has been through the Royal Society of Chemistry peer review process and has been accepted for publication.

Accepted Manuscripts are published online shortly after acceptance, before technical editing, formatting and proof reading. Using this free service, authors can make their results available to the community, in citable form, before we publish the edited article. We will replace this Accepted Manuscript with the edited and formatted Advance Article as soon as it is available.

You can find more information about Accepted Manuscripts in the author guidelines.

Please note that technical editing may introduce minor changes to the text and/or graphics, which may alter content. The journal's standard Terms & Conditions and the ethical guidelines, outlined in our author and reviewer resource centre, still apply. In no event shall the Royal Society of Chemistry be held responsible for any errors or omissions in this Accepted Manuscript or any consequences arising from the use of any information it contains.

ROYAL SOCIETY OF CHEMISTRY

rsc.li/nanoscale

View Article Online
DOI: 10.1039/C7NR01712J

Nanoscale RSCPublishing

ARTICLE

Published on 12 June 2017. Downloaded by University of California - San Diego on 12/06/2017 20:17:49.

Cite this: DOI: 10.1039/x0xx00000x

Received 00th January 2012,
Accepted 00th January 2012

DOI: 10.1039/x0xx00000x

www.rsc.org/

Controlled defect creation and removal in graphene and MoS_2 monolayers

D.W. Li,[±,a] Q.M. Zou,[±,a] X. Huang,[a] H. Rabiee Golgir,[a] K. Keramatnejad,[a] J.F. Song,[b,c] Z.Y. Xiao,[b,c] L.S. Fan,[a] X. Hong,[b,c] L. Jiang,[d] J.F. Silvain,[e] S. Sun,[b,c,f] and Y.F. Lu*[,a]

It is known that defects strongly influence the properties of two-dimensional (2D) materials. The controlled creation and removal of defects can be utilized to tailor the optical and electronic response of these 2D materials for optoelectronic and nanoelectronic applications. In this study, we developed an efficient approach to reversibly control the defect states in mechanically exfoliated graphene and molybdenum disulfide (MoS_2) monolayers. The defects were created by aluminium oxide (Al_2O_3) plasmas and removed by moderate thermal annealing at up to 300 ^{o}C. We employed Raman and photoluminescence (PL) as well as electrical characterizations to monitor the variation of the defect level in graphene and MoS_2. For graphene, Raman spectra indicate that the Al_2O_3 plasma induced sp^3-type defects with controlled concentration, which have been substantially removed after thermal annealing. Similar trend was also observed in monolayer MoS_2, as revealed by the defect-related emission peak (X^b) in the PL spectra. We further showed that the defects induced by the Al_2O_3 plasma in both 2D materials can be restored to any intended level via annealing with well-controlled conditions. Our work presents a new route to the functional design of the optical and electronic properties of graphene and MoS_2-based devices through defect engineering.

Nanoscale Accepted Manuscript

Introduction

Two-dimensional (2D) materials, especially graphene and transition metal dichalcogenide (TMD) semiconductors (such as molybdenum disulfide (MoS_2)), have attracted significant research and industrial interest due to their outstanding electronic and optical properties and wide potential applications for the next-generation of flexible field-effect transistors,[1,2] integrated logic circuits,[3] photodetectors and photovoltaic devices,[4-7] energy storage,[8,9] and sensors.[10,11] It has been well documented that defects significantly influence the properties of 2D materials.[12-18] Therefore, the controlled introduction of defects into these materials could tailor their optical, electrical, catalytic, and even magnetic properties.[19-23] Examples include the local enhancement of optical excitations at graphene edges,[24] generation of tunable magnetic phases in graphene with vacancies,[25,26] a strong enhancement photoluminescence from MoS_2 through defect engineering and oxygen bonding,[27] and the significant improvement in hydrogen evolution activity in MoS_2 through oxygen plasma exposure and annealing in hydrogen.[28]

Compared to the conventional approach, in which defects are unintentionally created during 2D material growth,[29] defect engineering through post-synthesis or direct modification offers better controllability over defect levels and types. To date, significant effort has been devoted to the modification of 2D materials through defect creation, including ion/electron beam irradiation,[30-38] plasma treatments,[14,39,40] UV light illumination,[41,42] and the sputtering of insulating layers.[43] Compared with the ion/electron beam and UV light irradiation, the controllability of defects in 2D materials by sputtering so far has not been extensively studied.

On the other hand, many methods have been developed to remove or heal the defects in 2D materials, which includes vapor phase treatment,[44] electrochemical deposition,[45] and thermal annealing.[31,43,46,47] Although vapor phase treatment and electrochemical deposition enabled the improvement of the electrical conductivity and mechanical properties, the defects in 2D materials could not be recovered. Thermal annealing is a promising approach for defect restoration. Guo and Zion et al. reported restoration of defects in graphene introduced by N^+ (or C^+) ion irradiation after annealing in nitrogen gas (N_2) (or vacuum).[31,46] However, an ultrahigh annealing temperature of 1000-1100 ^{o}C is required for defect repair; and full restoration of graphene structure is very difficult, where the maximal content restoration of defects relating to I_D/I_G can only be reduced to a minimum ~ 0.32 (from ~ 3.38 for irradiated sample). In addition, Ni et al. reported recovery of process-induced defects in graphene by annealing in air. However, a number of defects remained after annealing at 500 ^{o}C and the thin graphene was oxidized after annealing at 600 ^{o}C.[43] Recently, Imamura et al. realized restoration of UV-induced defects in graphene by annealing in vacuum at 160 ^{o}C.[41] While most of the studies mentioned above were focused on the defect engineering in graphene, other 2D materials, however, have not been fully explored.[48] Consequently, it is of high research interest to explore and develop a more efficient, cost-effective approach to realizing reversible defect engineering not only in graphene but also in other 2D materials, such as TMDs.

Aluminum oxide (Al_2O_3) has been widely used as high-k gate dielectric for 2D-material-based nanoelectronic devices, where atomic layer deposition (ALD) is a preferred method to deposit dielectric Al_2O_3 without introducing defects during the deposition.[49-53] However, to controllably modify 2D material in-plane via Al_2O_3 has hardly been studied. Here, we demonstrate, for the first time, that the sputtering of low-energy Al_2O_3 may induce controlled defects in both graphene and MoS_2 monolayers, while subsequent annealing at

View Article Online
DOI: 10.1039/C7NR01712J

Nanoscale RSCPublishing

ARTICLE

Published on 12 June 2017. Downloaded by University of California - San Diego on 12/06/2017 20:17:49.

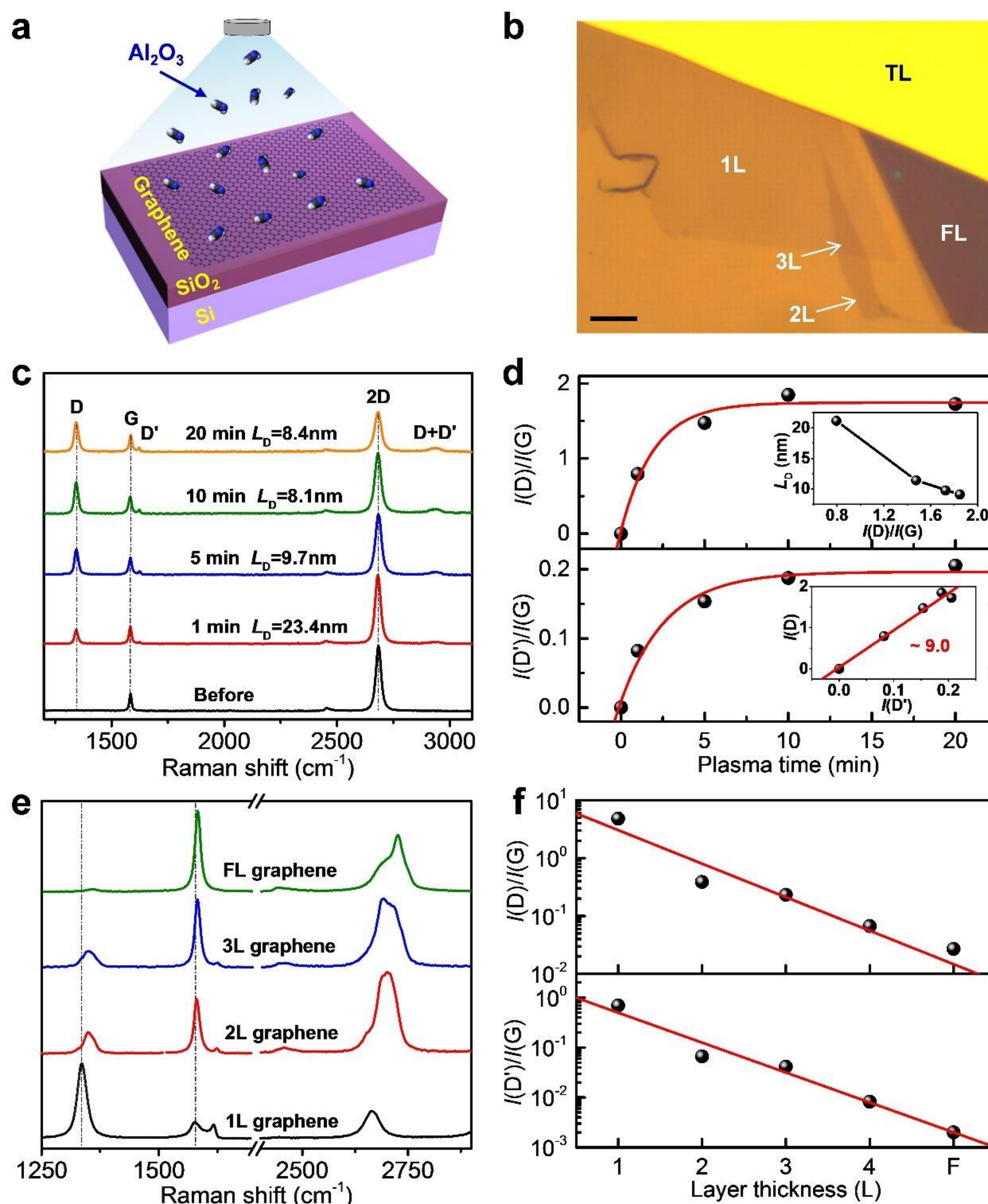

Fig. 1. Controlled creation of defects in graphene monolayer and few-layers. (a) Schematic of the generation of surface defects in a graphene film via Al_2O_3 plasma treatment. (b) Optical image of the as-prepared monolayer to few-layer graphene on SiO_2/Si substrate. Scale bar: 5 μm. (c) Raman spectra of an exfoliated monolayer graphene as a function of Al_2O_3 plasma treatment time, where the spectra are normalized to the intensity of the G peak. (d) The I_D/I_G (top) and $I_{D'}/I_G$ (bottom) ratio as a function of plasma time. Insets in (d) show the L_D with respect to I_D/I_G ratio (top) and I_D versus $I_{D'}$ (bottom). (e) Raman spectra of monolayer to few-layer graphene subjected to Al_2O_3 plasma for a fixed time of 10 min. (f) The I_D/I_G (top) and $I_{D'}/I_G$ (bottom) ratio as a function of layer thickness.

Nanoscale Accepted Manuscript

View Article Online
DOI: 10.1039/C7NR01712J

Nanoscale RSCPublishing

ARTICLE

Published on 12 June 2017. Downloaded by University of California - San Diego on 12/06/2017 20:17:49.

low temperatures can reverse the defect creation process, realizing a controlled defect creation and removal. Raman and photoluminescence (PL) spectra were used as reliable approaches to assess the defect levels and monitor the reversible defect engineering process in 2D monolayers. Based on the Raman, PL, and atomic force microscopy (AFM) characterizations, we proposed the possible mechanism and the potential of this defect engineering technique. The work presented here demonstrates an efficient approach for realizing the active control of defects in 2D materials and brings new opportunities for tailoring their properties and creating new functionalities. For example, our results can provide a guideline to design monolayer graphene-/TMD-based electronic devices with a controlled densities of defects or doping suitable for chemical sensing applications.

Experimental section

Sample fabrication

Atomically thin graphene and MoS_2 samples were prepared by microcleavage of natural bulk crystals (Graphene Supermarket) using Scotch® Transparent Tape, before being transferred onto 300 nm SiO_2/Si substrates. Briefly, 2D materials were first exfoliated onto a nonresidue polymer gel film (Gel-Pak Company) surface and then transferred onto a SiO_2/Si substrate. The SiO_2/Si substrates were cleaned with acetone and isopropanol and then rinsed with deionized water before receiving the exfoliated 2D materials. High-quality monolayer and few-layer flakes of sizes up to 20 μm were obtained using this method, which were initially identified from optical contrast using an optical microscopy.

Defect generation via Al_2O_3 plasma irradiation

Graphene and MoS_2 samples were treated by the sputtering of Al_2O_3 in a radio frequency (RF) sputtering system (ATC ORION) equipped with an RF magnetron generator (Matching Networks). The Al_2O_3 target was sputtered in Ar at a pressure of ~ 5.5 mTorr. The RF powers were ranging from 5 to 100 W and dwell times were ranging from 1 to 120 min. The thickness of Al_2O_3 thin film scales linearly with the time of sputtering (Supporting Information, Fig. S1), indicating a stable deposition rate.

Defect removal via moderate thermal annealing

Thermal annealing was performed in an atmospheric pressure chemical vapor deposition (CVD) system (MTI OTX-1200 dual zone furnace) at different temperatures (100 to 300 °C) for 30 min.

Raman, PL, and AFM measurements

Both Raman and PL measurements were performed at room temperature and atmospheric pressure in a micro-Raman system (Renishaw inVia Plus, Renishaw, Gloucetershire, UK). The Raman scattering was excited by a 514 nm Ar^+ laser with a power of ~ 200 μW, while the PL scattering was excited by a 633 nm He-Ne laser with a power of ~ 20 μW to avoid heating. The spot size of 633 nm laser beam focused onto the sample was ~ 1.5 μm, while the focal spot size for 785 nm laser beam was ~ 2 μm. Raman and PL spectra were collected through a 50× objective lens with an accumulation time of 10 s at each position. Renishaw WIRE 3.4 software was used to fit the Raman and PL spectra collected based on Gaussian-Lorentzian mixed profile. An AFM (Bruker Multimode 8 AFM) operated in the peak-force working mode was applied to determine the thickness of the sample and to study the morphological evolution in Al_2O_3-plasma-modified 2D materials.

Results and discussion

In this study, graphene as a typical 2D semimetal and MoS_2 as a typical 2D semiconductor were chosen as our research object. Graphene and MoS_2 monolayer and few-layer samples were mechanically exfoliated from commercially available bulk single crystals (Graphene Supermarket) onto 300 nm silicon dioxide/silicon (SiO_2/Si) substrates that were cleaned with acetone and isopropanol. We first studied defect engineering in exfoliated graphene monolayers (Fig. 1). To realize controlled defect creation, a piece of monolayer graphene (1LG) was exposed in Al_2O_3 plasmas for successive treatments of 1, 5, 10, and 20 min, at a pressure of ~ 5.5 mTorr and with a power of 5 W (Fig. 1a). By controlling the irradiation time, graphene with different levels of defects was obtained, which was monitored and quantitatively analyzed by Raman spectroscopy, as shown in Fig. 1c. All of the spectra exhibited two main features: the G-band at ~ 1579 cm^{-1}, arising from E_{2g} vibrational mode of sp^2 carbon network and the 2D-band at ~ 2668 cm^{-1}, corresponding to the overtone of the D-band. Before the plasma irradiation, the sample showed a typical Raman line with no trace of D-band, indicating that the pristine graphene was defect-free. After a very short irradiation time, two noticeable features induced by defects, the D-band at ~ 1336 cm^{-1} and the D'-band at ~ 1618 cm^{-1}, appeared in the spectra and increased with the exposure time (Fig. 1c). Fig. 1d shows the intensity ratio of the Raman D (D') to G-band [*i.e.*, I_D/I_G ($I_{D'}/I_G$)] as a function of the plasma time. Both the ratios of I_D/I_G and $I_{D'}/I_G$ increased monotonically when the Al_2O_3 plasma time was increased to 5 min, then increased gradually, and finally reached a maximum value (~ 1.8 for I_D/I_G and ~ 0.2 for $I_{D'}/I_G$) when the plasma time was further increased to 20 min. A similar trend was also observed in bilayer graphene (2LG) (Supporting Information, Fig. S2). The evolution of the aforementioned Raman features implies the controlled formation of defects in graphene induced by the weak Al_2O_3 plasma. According to the trends summarized by amorphization trajectory,[54,55] I_D/I_G increases when crystalline graphene evolves into a nanocrystalline phase (Stage I) and then decreases when nanocrystalline graphene becomes low sp^3 amorphous carbon (Stage II). Our case appears to follow the first stage of the amorphization trajectory, thus, the formation of the amorphous phase was avoided in the graphene irradiated with Al_2O_3 plasmas, even with a longer exposure time. We can, therefore, quantify the amount of defects in graphene after a series of irradiations using the well-known Tuinstra-Koenig relation:[56]

$$L_D = \left(2.4\times10^{-10}\right)\lambda^4\left(I_D/I_G\right)^{-1}, \quad (1)$$

where L_D is the size of in-plane crystallites and λ is the laser excitation wavelength. In our experiment (top insets in Figs. 1d and S2f), a long time exposure of Al_2O_3 plasma led to the formation of crystalline grain sizes on the order of ~ 8 nm (in 1LG) and ~ 19 nm

Nanoscale Accepted Manuscript

View Article Online
DOI: 10.1039/C7NR01712J
Published on 12 June 2017. Downloaded by University of California - San Diego on 12/06/2017 20:17:49.
Nanoscale Accepted Manuscript

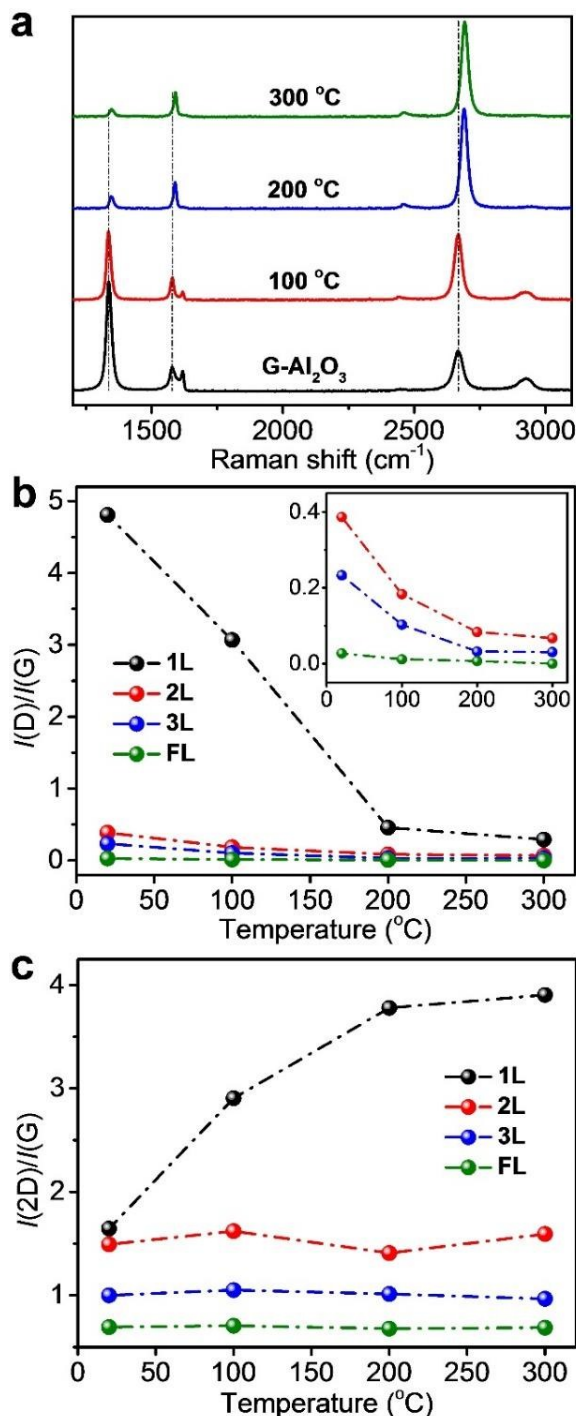

Fig. 2. Removal of surface defects in graphene induced by Al_2O_3 plasma. (a) Raman spectra of the defective monolayer graphene as a function of annealing temperature. (b,c) The dependence of (b) I_D/I_G and (c) I_{2D}/I_G ratio on the annealing temperature for plasma-treated monolayer to few-layer graphene. Insert in (b) shows the maginified curves for 2L, 3L, and FL graphene.

(in 2LG), which indicated well-controlled moderate density defects in our case.[30]

Considering the D-band represents many types of defects, the detailed mechanism of defect formation in graphene is still unclear.[57] In the present work, the defect formation via Al_2O_3 plasma treatment may be caused by the interaction between Al_2O_3 and graphene which may produce weak dangling bonds, sp^3-type defects, and/or vacancy-like defects. To confirm if the sputtered Al_2O_3 created weak dangling bonds with graphene, Al_2O_3 thin layer was etched using hydrofluoric acid (HF) dilute solution (DI water : HF = 100:1). However, the D-band still existed after Al_2O_3 removal (Supporting Information, Fig. S3), suggesting that the defects in Al_2O_3-treated graphene should not be dominated by the dangling bonds at the Al_2O_3/graphene interfaces. It has been reported that $I_D/I_{D'}$ can be used experimentally to obtain information on the nature of defects in graphene: $I_D/I_{D'} > 7$ for sp^3-type defects, while $I_D/I_{D'} < 7$ for vacancy-like defects.[57] Fig. 1d (bottom inset) and Fig. S2g plot I_D versus $I_{D'}$ for 1LG and 2LG, respectively, where $I_D/I_{D'} = B$ (~ 9.0 for 1LG and ~ 7.1 for 2LG) higher than 7. B is a constant and should not depend on defect density but only on the type of defect. This indicates that defects associated with sp^3 hybridization were mainly created in the graphene by Al_2O_3 plasma treatments with low power (5W), suggesting the low defect concentration level.[57,58]

We further investigated the effect of plasma irradiation on graphene of different layer thicknesses. A single sample containing 1L-, 2L-, 3L-, and FL-graphene (FLG) was selected (Fig. 2b and Fig. S4a) and irradiated by the plasma under the same conditions. Fig. 1e compares the Raman spectra from the Al_2O_3-treated graphene samples of different layer thicknesses and shows that FLG was less disordered than 1LG, indicating that the effect of Al_2O_3 plasma on the thicker samples weakened. This is consistent with the previous work,[59] and can be understood that only the top layer of graphene was modified, while the bottom layer maintained its original structure.[60] It should be noted that the estimation of the number of defects in multilayered graphene based on the D (D') band intensity can result in an overestimation due to the scattering of phonons in the bottom layer by defects in the top layer.[58] To simplify the discussion, we ignored this effect in our work. As shown in Fig. 1f, both the I_D/I_G and $I_{D'}/I_G$ intensity ratios decreased exponentially as the layer thickness increased, which suggested that the defect level was inversely proportional to the thickness. The I_D/I_G ($I_{D'}/I_G$) as a function of the layer thickness can be fitted with an equation as:

$$I_{D(D')}/I_G = \left(I_{D(D')}/I_G\right)_{sat} e^{-aN}, \tag{2}$$

where $(I_{D(D')}/I_G)_{sat}$ is the ratio at its saturation value, N is the number of layers, and the parameter a is defined as the disorder release efficiency. By fitting the data, we found that I_D/I_G had the same a (~ 0.58) as that of $I_{D'}/I_G$. This indicated that the parameter a does not depend on the defect concentration and the irradiation time but only depends on the plasma energy. Another interesting observation in Fig. 1e is that the D-band in the Al_2O_3-irradiated 1LG (~ 1336.5 cm^{-1}) was red-shifted by ~ 16 cm^{-1} compared to that of 2L-FLG (~1352 cm^{-1}). We attribute this significant red shift of the D-band to the strong tensional stress on atomic thin 1LG as a result of depositing Al_2O_3 with a larger lattice constant than graphene. In contrast, the G-band of 1L to FL graphene did not show a noticeable shift after Al_2O_3 modification (Supporting Information, Fig. S4b).

The Al_2O_3-irradiated samples (Fig. 1e) were then thermally annealed in argon (Ar) from 100 to 300 °C for 30 min at each temperature (Fig. 2, Supporting Information, Fig. S5). One can see that, after annealing at lower temperatures, *i.e.*, 100 and 200 °C, the D-band and I_D/I_G ratios were significantly reduced to different levels while the D'-band could almost be removed during this process (Figs. 2a and 2b), indicating the restoration of the lattice structures, that is, Al_2O_3-irradiated 1LG with the sp^3-type defects changed into sp^2-bonded graphene after the low-temperature annealing. When the temperature increased to 300 °C, the intensity ratio of I_D/I_G decreased from ~ 4.8 (before annealing) to ~ 0.29 for 1LG, which was even lower for the thicker samples (Fig. 2b). In our case, the restoration of graphene structure obtained at low annealing temperatures was even better than that Guo et al. obtained at ultra-

This journal is © The Royal Society of Chemistry 2012

View Article Online
DOI: 10.1039/C7NR01712J

Nanoscale RSCPublishing

ARTICLE

Published on 12 June 2017. Downloaded by University of California - San Diego on 12/06/2017 20:17:49.

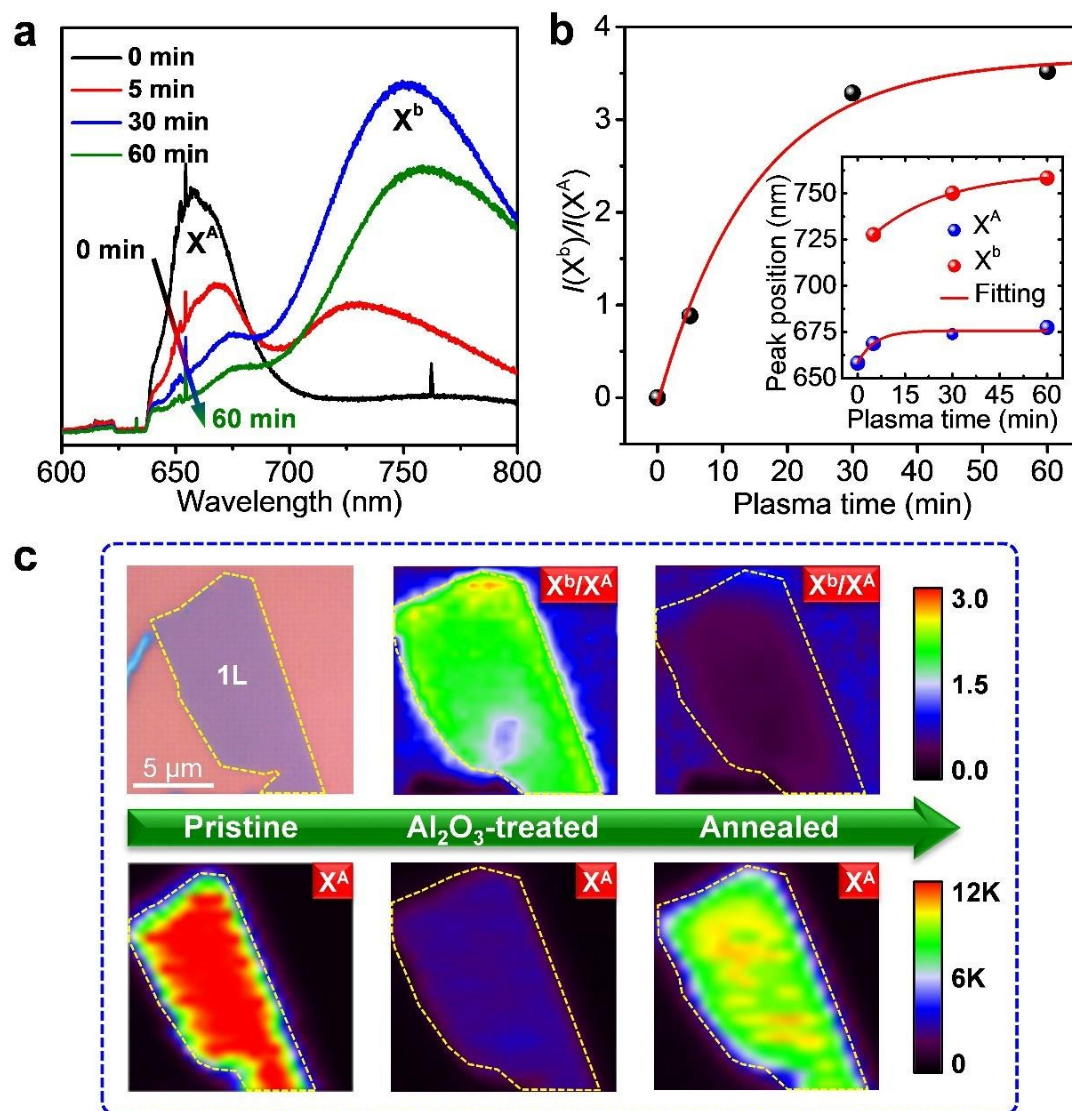

Fig. 3. Controlled creation of defects in 1L-MoS_2. (a) PL spectra of an exfoliated 1L-MoS_2 with increasing Al_2O_3 plasma treatment time. (b) The intensity ratio of X^b/X^A as a function of plasma exposure time. Inset in (b) shows the neutral (X^A) and defect-bound (X^b) exciton peak position as a function of plasma exposure time. (c) PL mapping characterization: optical image (top left) and X^A intensity mapping (bottom left) of the pristine 1L-MoS_2, X^b/X^A intensity ratio (top) and X^A intensity (bottom) mapping for the Al_2O_3-treated same sample before (middle) and after (right) annealing at 300 °C.

high annealing temperatures (1100 °C).[31] It is known that the intensity ratio of I_{2D}/I_G can be considered as a measure of the non-destroyed part of the graphene lattices.[46] Fig. 2c shows the dependence of I_{2D}/I_G on the annealing temperature. For 1LG, the annealing treatment led to an increase of the I_{2D}/I_G ratio from ~ 1.64 (before annealing) to ~ 3.9 (after annealing at 300 °C). This value was almost equal to that of the pristine sample. However, no noticeable changes were observed for the I_{2D}/I_G ratios in the graphene bilayer to few-layers, which suggests that I_{2D}/I_G cannot be used as a sensitive indicator for the "state of defectiveness" in few-layer graphene.

Another interesting observation is that G- and 2D-bands in Al_2O_3-treated 1LG significantly blue-shifted as the annealing temperature increased (Supporting Information, Fig. S6a), where the G-band blue shifted ~ 12.0 cm^{-1} and 2D-band blue-shifted ~ 25.1 cm^{-1} after annealing at 300 °C. Similar to the previous reports,[43] the blue shift of Raman bands can be attributed to the strong compressive stress on the graphene. After thermal annealing, Al_2O_3 recrystallized, leading to denser film and imposing to a compressive stress on the graphene underneath. The morphological changes of Al_2O_3 will be discussed in a later section. Besides the blue shift of G- and 2D- bands, there was a significant FWHM (full width at half-maximum) narrowing

Nanoscale Accepted Manuscript

View Article Online
DOI: 10.1039/C7NR01712J

Nanoscale RSCPublishing

ARTICLE

Published on 12 June 2017. Downloaded by University of California - San Diego on 12/06/2017 20:17:49.

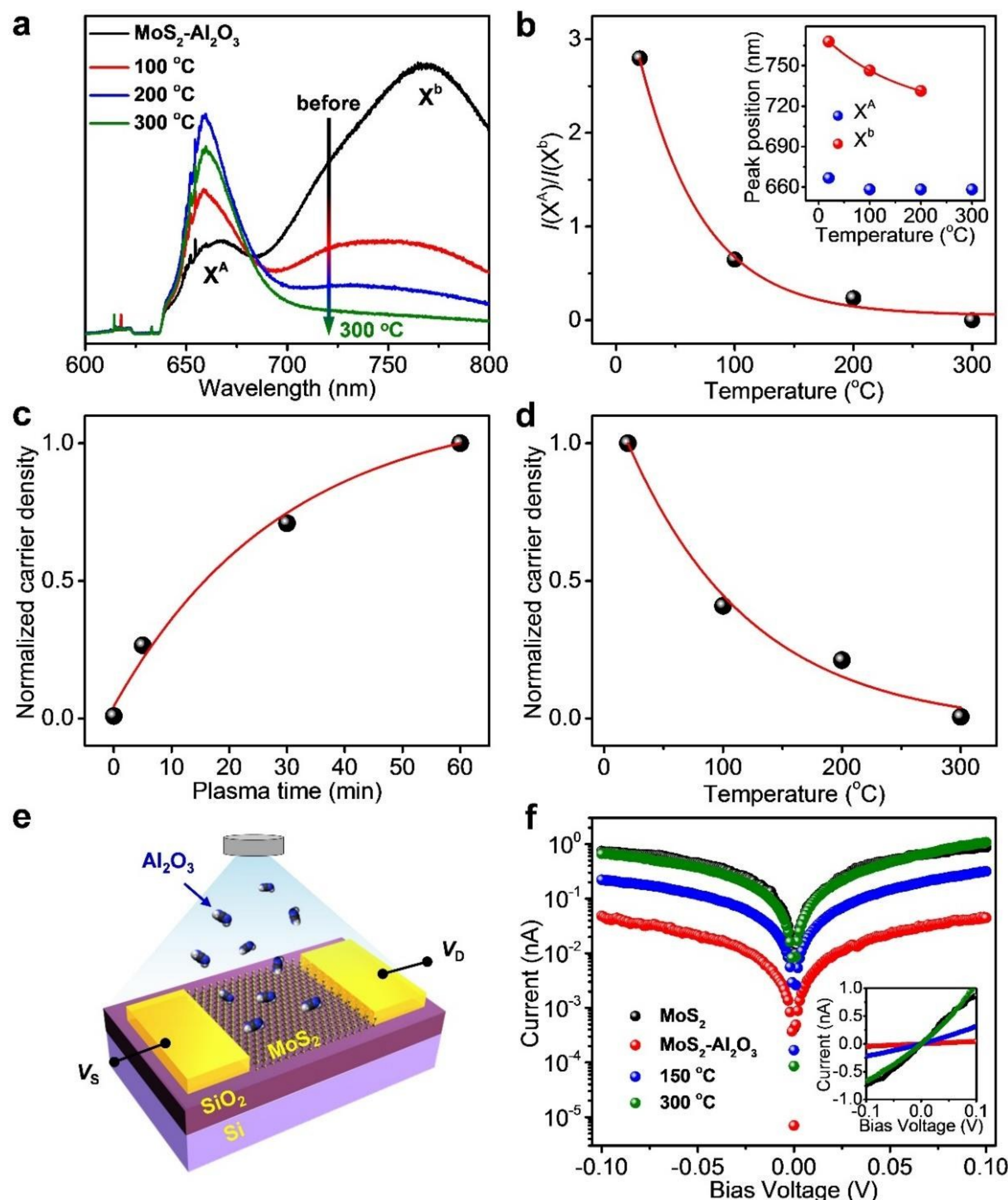

Fig. 4. Removal of Al_2O_3-plasma-induced defects in 1L-MoS_2. (a) PL spectra of the defective 1L-MoS_2 after thermal annealing at various temperatures. (b) The X^b/X^A intensity ratio as a function of annealing temperature. Inset in (b) shows the exciton (X^A) and defect-bound exciton (X^b) peak position as a function of annealing temperature. (c,d) Normalized carrier density in 1L-MoS_2 as a function of the (c) Al_2O_3 plasma treatment time and (d) annealing temperature. (e) Schematic of a 1L-MoS_2 device on SiO_2/Si substrate with two-probe geometry. (f) *I-V* output characteristics (logarithmic) of the pristine 1L-MoS_2 (black), Al_2O_3-plasma-treated 1L-MoS_2 before (red) and after being annealed at 150 °C (blue) and 300 °C (green), where the same data shown in linear scale is inserted at the bottom right.

for both G- and 2D-bands after annealing at different temperatures (Supporting Information, Fig. S6b), which was similar to the case of charge doping as reported by Yan et al.[61] This indicated that the defect-associated doping possibly existed in the graphene, which could be restored by annealing. After annealing at 300 °C, the FWHM of both G- and 2D-bands decreased to a small value close to

Nanoscale Accepted Manuscript

View Article Online
DOI: 10.1039/C7NR01712J

Published on 12 June 2017. Downloaded by University of California - San Diego on 12/06/2017 20:17:49.

that of the pristine graphene, further demonstrating that most of the defects and the doping effect in 1LG were removed at such low annealing temperature. Summarizing, in combination of moderate Al_2O_3 plasma treatments and low-temperature annealing, the defect creation and removal in the whole graphene surface was realized in a controllable manner (Supporting Information, Fig. S7).

We also applied the same Al_2O_3 plasma treatments as those employed for graphene to manipulate the defect level in semiconductor 2D TMDs, where monolayer MoS_2 (1L-MoS_2) was chosen as a typical example. PL spectroscopy has been developed as a reliable approach to assessing the quality of TMD samples under ambient conditions (room temperature and atmospheric pressure).[14] Fig. 3a shows the room-temperature PL spectra for 1L-MoS_2 with different Al_2O_3 plasma times. The pristine 1L-MoS_2 showed a strong PL emission with the characteristic peak at ~ 655 nm (~ 1.89 eV) from the neutral X^A exciton. As the sample was exposed to Al_2O_3 plasma for a very short time (~ 5 min), a new spectral feature at ~ 729 nm (~ 1.70 eV), located ~ 190 meV below the X^A exciton peak, rose in the PL spectrum. We attribute this feature to the defect-bound exciton (X^b),[14] associated with the radiative recombination of excitons bound to defect sites, which can be used to determine the defect level in 1L-MoS_2. The location of the X^b exciton below the X^A exciton indicated that defects created by the Al_2O_3 plasma acted as exciton traps, which reduced the electron-hole pair interaction. With the increase in the plasma irradiation time, the intensity of X^b exciton consistently increased while the X^A exciton steadily decreased, suggesting the increase of the defect densities in 1L-MoS_2. The decrease in X^A along with the increase in X^b also implied irradiation-induced conversion from neutral (X^A) to defect-bound (X^b) excitons.

The X^b/X^A intensity ratio was obtained to quantify defect levels, as shown in Fig. 3b. It can be seen that X^b/X^A ratio showed a parabolic rise with the irradiation time, similar to the trend obtained in graphene by a Raman intensity ratio of I_D/I_G, demonstrating that the weak Al_2O_3 plasma is capable of controllably introducing defects in 1L-MoS_2 by tuning the processing time. On the other hand, no obvious changes were observed in the Raman spectra of 1L-MoS_2 as a function of the Al_2O_3 plasma time (Supporting Information, Fig. S8b), indicating that Raman spectra are not sensitive to the defects induced by the weak Al_2O_3 plasmas. To confirm this Raman result, we studied the role of Al_2O_3 plasma power on the Raman spectra of 1L-MoS_2 (Supporting Information, Fig. S8c), where high-power (100 W) Al_2O_3 plasma irradiation induced an obvious evolution of both linewidth and frequency shifts of the Raman features.[62] The inset in Fig. 3b shows the peak positions of X^A and X^b plotted versus the irradiation time. It is clear that the X^A peak rapidly red-shifted after 5 min of plasma treatment and then saturated at a certain irradiation time, meanwhile the X^b peak gradually red-shifted and then reached a maximum with successive plasma irradiation, indicating defect site saturation with trapped excitons after a long period of Al_2O_3 plasma treatments. We also investigated the spatial distribution of the Al_2O_3-plasma-induced defects by measuring the PL mapping (Fig. 3c). The X^A peak intensity mapping for the pristine 1L-MoS_2 showed uniform distribution (Fig. 3c, bottom left). For the same sample after plasma treatment for 10 min, the mapping of X^b/X^A ratio (Fig. 3c, top middle) and X^A peak intensity (Fig. 3c, bottom middle) clearly showed a significant and uniform irradiation-induced conversion from neutral (X^A) to defect-bound (X^b) excitons, suggesting that the Al_2O_3-plasma-induced defects were uniformly distributed on the whole monolayer surfaces.

Then, we investigated the possibility of removing defects in the Al_2O_3-plasma-irradiated 1L-MoS_2 by annealing at low temperatures. Fig. 4a shows the changes in PL spectra for the defective 1L-MoS_2 after it was annealed in Ar at different temperatures. One can see that, the PL was dominated by the X^b emission prior to annealing, implying a high defect concentration. After annealing at 100 ºC, we observed a significant decrease (increase) in the X^b (X^A) emission (Fig. 4b), associated with a decrease in the X^b/X^A intensity ratio from ~ 2.8 to ~ 0.6, which suggested annealing-induced conversion from defect-bound exciton to neutral exciton emission. It was noted that longer annealing times than 30 min at this temperature caused little further change in each emission contribution to PL. After 200 ºC annealing, the X^b (X^A) emission further decreased (rose), indicating a well-controlled restoration of the lattice structures. Surprisingly, after annealing at 300 °C, the X^b emission contribution could no longer be seen; and the intensity of X^A remained relatively stable. This implied that the defects in 1L-MoS_2 were reduced and close to their original state. The mapping of X^b/X^A ratio (top right) and X^A peak intensity (bottom right) in Fig. 3c confirmed that annealing at 300 ºC removed most of the defects on the whole sample surfaces. Additionally, we observed that both the X^A and X^b bands blue-shifted with the annealing process and saturated after a certain annealing temperature (Fig. 4b inset), which was considered as another signature of restoration of the lattice structure in MoS_2.

It has been reported that the PL intensity and peak positon of 1L-MoS_2 exhibit a strong dependence on carrier doping.[63] In the present work, the redshift of X^A (X^b) peak after Al_2O_3 sputtering could be attributed to the defect-associated *n*-type doping in 1L-MoS_2, while the X^A (X^b) peak blue shift after subsequent annealing indicated an effective doping removal. The carrier doping is also known to be an effective method to modify the carrier densities of 2D monolayers.[63,64] Thus, we investigated the evolution of carrier densities of 1L-MoS_2 at different processing stages. The carrier density can be estimated by

$$n_i^2 \propto exp(-\frac{E_g}{k_B T}), \quad (3)$$

where E_g is the band gap related to the PL X^B peak, k_B is the Boltzmann constant, and T is the Kelvin temperature. Fig. 4c showed the normalized carrier density as a function of Al_2O_3 sputtering time, which increased parabolically due to a larger number of defect-induced doping. In contrast, the carrier density of Al_2O_3-treated 1L-MoS_2 exhibited an exponential decrease after thermal annealing (Fig. 4d). This behavior was similar to the change of X^b/X^A intensity ratio as a function of sputtering time and annealing temperature. These results suggested that a reversible control of both the defects and the doping level in 1L-MoS_2 can be realized via a combination of Al_2O_3 sputtering and post annealing technique.

As further confirmation of the controlled defect creation and removal in 1L-MoS_2, we investigated the effects of Al_2O_3 plasma irradiation and post annealing on the electrical performance of 1L-MoS_2 devices. Previous studies showed that the electrical properties of MoS_2 were highly influenced by the introduction of defects,[15,16,65,66] leading to significant degradation of the electrical performances. Fig. 4e shows a schematic of 1L-MoS_2 device on SiO_2/Si substrate with two-probe geometry. Standard photolithography and e-beam evaporation were used to form the Ti/Au (5/50 nm) contacts as the source and drain electrodes. In this experiment, we examined the change in current-voltage (*I-V*) characteristics of a 1L-MoS_2 device of length ~ 5 µm and width ~ 11 µm at various stages: after Al_2O_3 plasma irradiation and after subsequent annealing at different temperatures (Fig. 4f). After Al_2O_3 irradiation for 5 min, the current decreased significantly by over an order of magnitude from ~ 1 nA to ~ 40 pA (V_{DS} = 1 V, V_g = 0 V). The reduction in electrical conductivity implied the formation of defects in the 1L-MoS_2 channel. After annealing at 150 °C, we observed a dramatic increase in the current, suggesting that the defects were partially removed. After further annealing at 300 °C,

Nanoscale Accepted Manuscript

View Article Online
DOI: 10.1039/C7NR01712J

Nanoscale

RSCPublishing

ARTICLE

Published on 12 June 2017. Downloaded by University of California - San Diego on 12/06/2017 20:17:49.

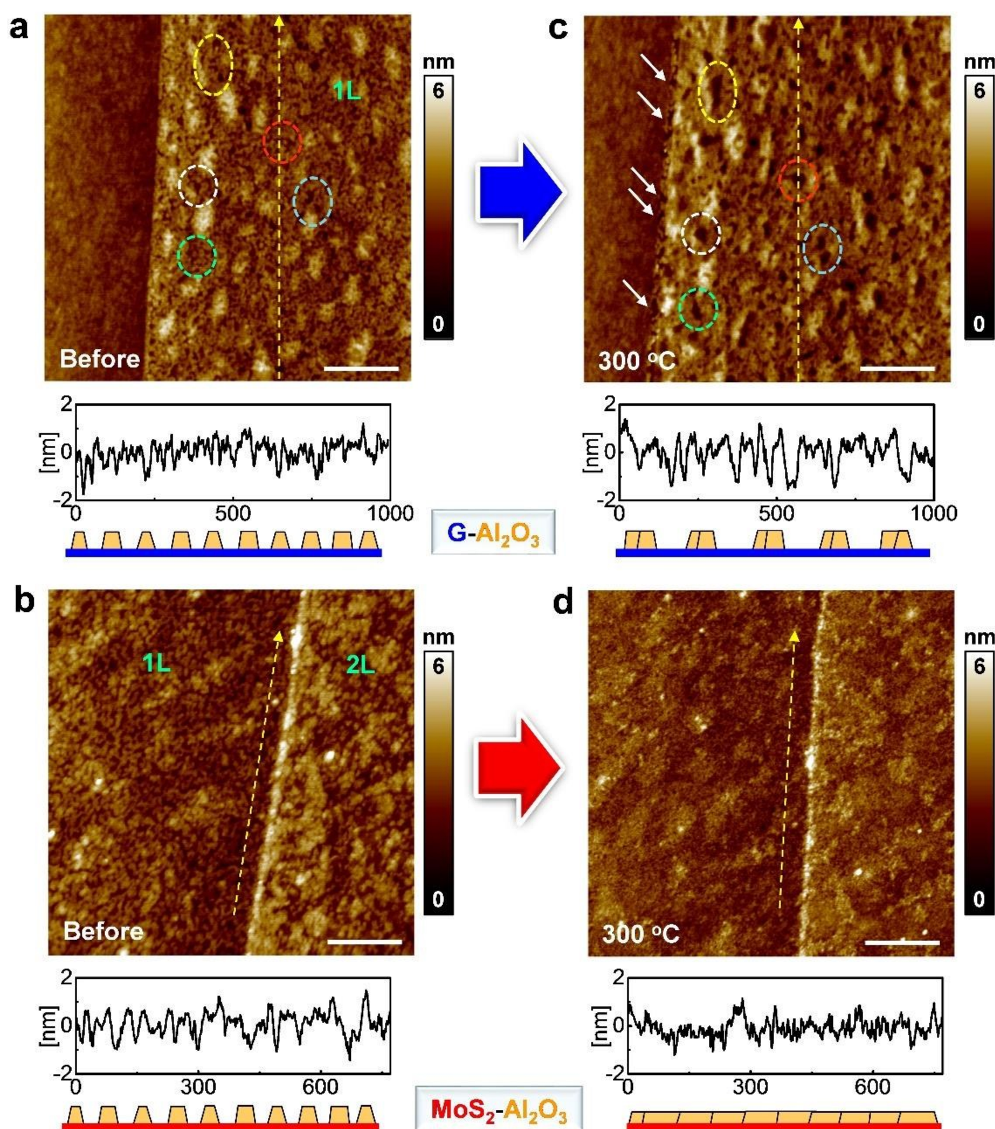

Fig. 5. *In situ* structural characterization of the ultrathin Al_2O_3-coated 2D monolayers. AFM topography images of ~ 1-nm-thick Al_2O_3-coated (a) 1LG and (b) 1L/2L-MoS_2 before annealing, and (c) 1LG and (d) 1L/2L-MoS_2 after annealing at 300 °C. Scale bars: 200 nm. Top insets in (a-d) show the corresponding cross-sectional profiles along the yellow dotted lines and bottom insets are the schematics of Al_2O_3 structural evolution on top of the 2D layers.

the current was restored to its original value, further demonstrating that the Al_2O_3-plasma-induced defects in 1L-MoS_2 were removed at such a low annealing temperature.

We used AFM to further investigate the structural evolution in the Al_2O_3-deposited 2D material surfaces to understand the changes in defect density throughout the whole defect engineering process. In this experiment, the sputtering of Al_2O_3 with a power of 5 W was performed for 5 min; and the thickness of the Al_2O_3 deposition on top was measured to be ~ 1 nm (Supporting Information, Fig. S9). The topographic surface images of the Al_2O_3-deposited 1LG and 1L-MoS_2 before annealing are shown in Figs. 5a and 5b, respectively. One can see that a non-uniform film with many uncovered regions (or nano-vacancies) was formed on both the graphene (Fig. 5a) and MoS_2 (Fig. 5b) surfaces. This is considered to be caused by the lack of available sites for the physical or chemical sorption of Al_2O_3 on their surfaces.[49] Therefore, the initial Al_2O_3 attached to a 2D crystal surface during the sputtering process was easily detached via thermal desorption, leading to a non-uniform and rough film morphology with many vacancies. Before annealing, the average density and diameter of the vacancies for 1LG were ~ 533.2 μm^{-2} and ~ 18.5 nm,

Nanoscale Accepted Manuscript

View Article Online
DOI: 10.1039/C7NR01712J

Nanoscale RSCPublishing

ARTICLE

Published on 12 June 2017. Downloaded by University of California - San Diego on 12/06/2017 20:17:49.

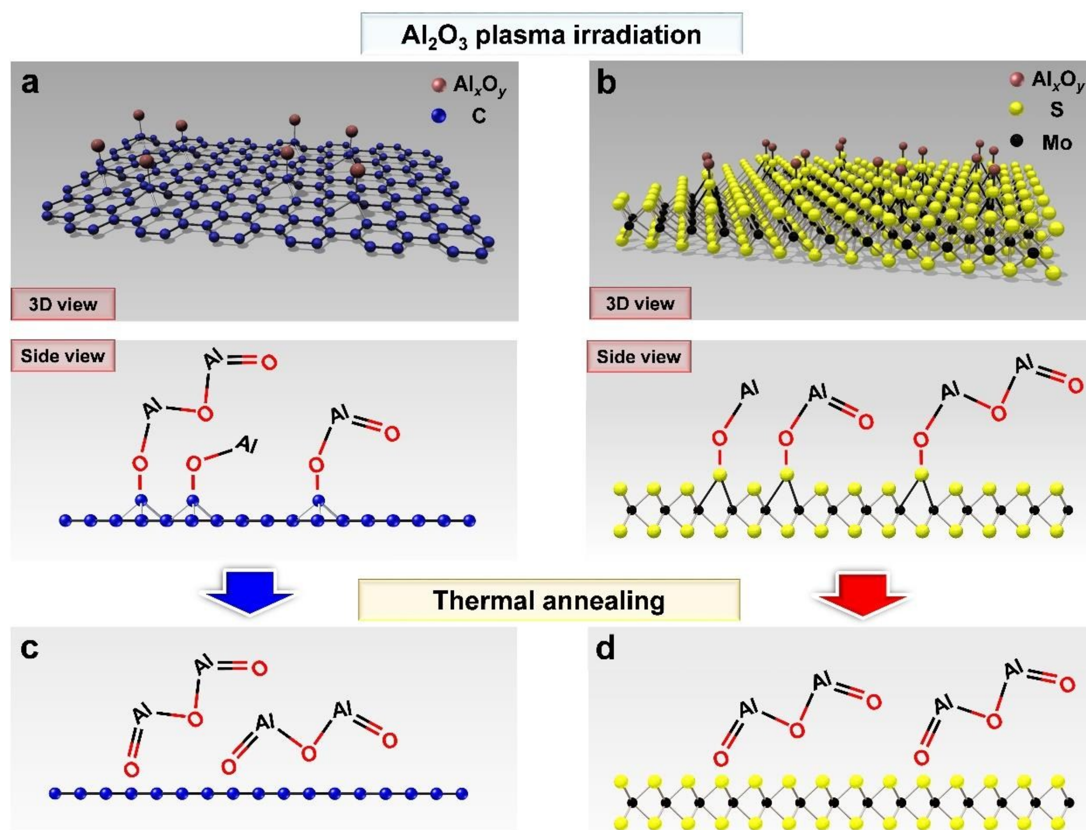

Fig. 6. Schematics of (a,b) defect creation by Al_2O_3 plasma irradiation in the monolayer (a) graphene and (b) MoS_2, and (c,d) defect removal by low-temperature thermal annealing in the Al_2O_3 plasma treated monolayer (c) graphene and (d) MoS_2.

respectively, which were calculated using a "Nano Scope Analysis" software. Interestingly, after 300 °C annealing treatments, the vacancy density dropped drastically (~ 344.1 μm^{-2}), which led to the formation of variously shaped larger vacancies on both the edge and in-plane regions (see arrows and dotted circles in Fig. 5c). The large and different shaped vacancies might be formed by a localized grain-grain coalescence during the annealing process (bottom inset in Fig. 5c), leading to a denser Al_2O_3 thin layer. This also indirectly explained the blue shift of G- and 2D-bands in Al_2O_3-treated 1LG after annealing. Similar behavior was also observed for the 2L and 3L graphene samples (Supporting Information, Fig. S10). On the contrary, for MoS_2 samples, both the density and diameter of the vacancies were significantly reduced after annealing (Figs. 5c and 5d), forming a smooth and uniform Al_2O_3 thin film on the MoS_2 surface (bottom inset in Fig. 5d). The different behaviors of Al_2O_3 evolution on graphene and MoS_2 are still not very clear and will be studied in our future work.

Based on the Raman, PL, and AFM results, we proposed a general defect creation and removal mechanism in the graphene and MoS_2 monolayers by weak Al_2O_3 plasma treatment and moderate thermal annealing (Fig. 6). With regard to the defects induced by Al_2O_3 plasmas, sp^3-type defects were considered to be formed, as evidenced by Raman analyses (Fig. 1). During the sputtering of Al_2O_3 (O=Al−O−Al=O), imperfect Al_xO_y structures with oxygen-enriched radicals were produced, which possibly include O=Al−O−Al−O·, O=Al−O·, ·Al−O·, and ·O−Al−O−Al−O·. These radicals could react with the graphene and MoS_2 and create sp^3-type defects in both 2D materials (Figs. 6a and 6b). More specifically, the sp^3-type defects in the graphene lattice arose from the carbon-oxygen (C−O) bonds, and the sulfur-oxygen (S−O) bonds were formed on the MoS_2 surfaces. With increasing in the sputtering time, the coverage area of Al_xO_y became higher, leading to the creation of more sp^3-type defects, as evidenced by Raman and PL spectra (Figs. 1 and 3). At some extent of sputtering process, the whole 2D surfaces were covered by Al_xO_y, which was the reason behind the defect saturation. It has been reported that the sp^3-type bonds, e.g., C−H and C−O, could possibly be broken by thermal annealing at < 200 °C.[41,67] In the present work, the restoration of defects to the pristine crystal lattices by thermal annealing could be explained by the detachment of oxygen on the 2D surfaces by breaking sp^3-type bonds (C−O in graphene and S−O in MoS_2) (Figs. 6c and 6d). Overall, our work provides a new approach for reversible defect engineering of 2D materials in a controllable manner, which is promising for producing next-generation 2D-based multifunctional devices for various applications.

Nanoscale Accepted Manuscript

Published on 12 June 2017. Downloaded by University of California - San Diego on 12/06/2017 20:17:49.

Nanoscale Accepted Manuscript

Conclusions

In summary, we have demonstrated controlled defect creation and removal in graphene and MoS_2 monolayers. The defects were created by weak Al_2O_3 plasma treatments and removed by moderate thermal annealing, as evidenced by room-temperature Raman and PL measurements. By irradiating both graphene and MoS_2 with Al_2O_3 plasmas under different conditions, these 2D materials with certain defect levels can be obtained. Interestingly, the subsequent moderate annealing can reverse the defect creation process, realizing a fully controlled defect engineering. The restored 2D materials have regained their superior performances in both structural and electrical conductivity. We proposed a general model for the Al_2O_3-plasma-treated 2D monolayers, where *sp*^{3}-type defects were mainly created at the interfaces between the Al_2O_3 and 2D monolayers, and the subsequent moderate annealing could remove such defects to restore their pristine crystal lattices. Thus, the precision and reversible defect engineering presented in this work opens a new avenue to tailoring their properties for the development of 2D-materials-based devices with new functionalities.

Acknowledgements

This research was financially supported by the National Science Foundation (CMMI 1265122), the Department of Energy [NETL: DE-FE0023061, BES: DE-FOA-00001032, BES: DE-SC0016153 (scanning probe studies)], the Nebraska Center for Energy Science Research, the National Key R&D Program of China (2016YFB0400801), the National Natural Science Foundation of China (61404147), and the Key Technology Research and Development Program of Jiangsu Province (BE2014147-1).

Notes and references

[a] *Department of Electrical and Computer Engineering, University of Nebraska-Lincoln, NE 68588-0511, United States. E-mail: ylu2@unl.edu.*

[b] *Department of Physics and Astronomy, University of Nebraska-Lincoln, Lincoln, NE 68588-0511, United States*

[c] *Nebraska Center for Materials and Nanoscience, University of Nebraska-Lincoln, NE 68588-0299, United States*

[d] *School of Mechanical Engineering, Beijing Institute of Technology, Beijing, 100081, China*

[e] *Institut de Chimie de la Matière Condensée de Bordeaux, Avenue du Docteur Albert Schweitzer F-33608 Pessac Cedex, France*

[f] *National Laboratory for Infrared Physics, Shanghai Institute of Technical Physics, Chinese Academy of Sciences, Shanghai, 200083, China*

[±] D.W. Li and Q.M. Zou contributed equally to this work.

† Electronic Supplementary Information (ESI) available. See DOI: 10.1039/b000000x/

1. B. J. Kim, H. Jang, S.-K. Lee, B. H. Hong, J.-H. Ahn and J. H. Cho, *Nano Lett.*, 2010, **10**, 3464-3466.
2. G.-H. Lee, Y.-J. Yu, X. Cui, N. Petrone, C.-H. Lee, M. S. Choi, D.-Y. Lee, C. Lee, W. J. Yoo and K. Watanabe, *ACS Nano*, 2013, **7**, 7931-7936.
3. H. Wang, L. Yu, Y.-H. Lee, Y. Shi, A. Hsu, M. L. Chin, L.-J. Li, M. Dubey, J. Kong and T. Palacios, *Nano Lett.*, 2012, **12**, 4674-4680.
4. F. Xia, T. Mueller, Y.-m. Lin, A. Valdes-Garcia and P. Avouris, *Nat. Nano.*, 2009, **4**, 839-843.
5. M.-L. Tsai, S.-H. Su, J.-K. Chang, D.-S. Tsai, C.-H. Chen, C.-I. Wu, L.-J. Li, L.-J. Chen and J.-H. He, *ACS Nano*, 2014, **8**, 8317-8322.
6. O. Lopez-Sanchez, D. Lembke, M. Kayci, A. Radenovic and A. Kis, *Nat. Nano.*, 2013, **8**, 497-501.
7. C. X. Guo, H. B. Yang, Z. M. Sheng, Z. S. Lu, Q. L. Song and C. M. Li, *Angew. Chem. Int. Edit.*, 2010, **49**, 3014-3017.
8. M. Pumera, *Energy Environ. Sci.*, 2011, **4**, 668-674.
9. T. Stephenson, Z. Li, B. Olsen and D. Mitlin, *Energy Environ. Sci.*, 2014, **7**, 209-231.
10. W. Li, X. Geng, Y. Guo, J. Rong, Y. Gong, L. Wu, X. Zhang, P. Li, J. Xu, G. Cheng, M. Sun and L. Liu, *ACS Nano*, 2011, **5**, 6955-6961.
11. F. K. Perkins, A. L. Friedman, E. Cobas, P. Campbell, G. Jernigan and B. T. Jonker, *Nano Lett.*, 2013, **13**, 668-673.
12. O. V. Yazyev and S. G. Louie, *Nat. Mater.*, 2010, **9**, 806-809.
13. Y. Wei, J. Wu, H. Yin, X. Shi, R. Yang and M. Dresselhaus, *Nat. Mater.*, 2012, **11**, 759-763.
14. P. K. Chow, R. B. Jacobs-Gedrim, J. Gao, T.-M. Lu, B. Yu, H. Terrones and N. Koratkar, *ACS Nano*, 2015, **9**, 1520-1527.
15. J. Hong, Z. Hu, M. Probert, K. Li, D. Lv, X. Yang, L. Gu, N. Mao, Q. Feng, L. Xie, J. Zhang, D. Wu, Z. Zhang, C. Jin, W. Ji, X. Zhang, J. Yuan and Z. Zhang, *Nat. Commun.*, 2015, **6**, 6293.
16. H. Qiu, T. Xu, Z. Wang, W. Ren, H. Nan, Z. Ni, Q. Chen, S. Yuan, F. Miao and F. Song, *Nat. Commun.*, 2013, **4**, 2642.
17. D. W. Li, Y. S. Zhou, X. Huang, L. Jiang, J. F. Silvain and Y. F. Lu, *Nanoscale*, 2015, **7**, 3651-3659.
18. D. Li, Z. Xiao, H. R. Golgir, L. Jiang, V. R. Singh, K. Keramatnejad, K. E. Smith, X. Hong, L. Jiang, J.-F. Silvain and Y. Lu, *Adv. Electron. Mater.*, 2017, 1600335-n/a.
19. K. Kim, J.-Y. Choi, T. Kim, S.-H. Cho and H.-J. Chung, *Nature*, 2011, **479**, 338-344.
20. F. Schedin, A. Geim, S. Morozov, E. Hill, P. Blake, M. Katsnelson and K. Novoselov, *Nat. Mater.*, 2007, **6**, 652-655.
21. Z. Yin, S. Sun, T. Salim, S. Wu, X. Huang, Q. He, Y. M. Lam and H. Zhang, *ACS Nano*, 2010, **4**, 5263-5268.
22. K. S. Novoselov, A. K. Geim, S. V. Morozov, D. Jiang, Y. Zhang, S. V. Dubonos, I. V. Grigorieva and A. A. Firsov, *Science*, 2004, **306**, 666-669.
23. D. Li, W. Xiong, L. Jiang, Z. Xiao, H. Rabiee Golgir, M. Wang, X. Huang, Y. Zhou, Z. Lin, J. Song, S. Ducharme, L. Jiang, J.-F. Silvain and Y. Lu, *ACS Nano*, 2016, **10**, 3766-3775.
24. W. Zhou, S. J. Pennycook and J.-C. Idrobo, *Ultramicroscopy*, 2012, **119**, 51-56.
25. X. Hong, K. Zou, B. Wang, S. H. Cheng and J. Zhu, *Phys. Rev. Lett.*, 2012, **108**, 226602.
26. J.-H. Chen, L. Li, W. G. Cullen, E. D. Williams and M. S. Fuhrer, *Nat. Phys.*, 2011, **7**, 535-538.
27. H. Nan, Z. Wang, W. Wang, Z. Liang, Y. Lu, Q. Chen, D. He, P. Tan, F. Miao and X. Wang, *ACS Nano*, 2014, **8**, 5738-5745.
28. G. Ye, Y. Gong, J. Lin, B. Li, Y. He, S. T. Pantelides, W. Zhou, R. Vajtai and P. M. Ajayan, *Nano Lett.*, 2016, **16**, 1097-1103.
29. S.-M. Lee, J.-H. Kim and J.-H. Ahn, *Mater. Today*, 2015, **18**, 336-344.
30. L. G. Cançado, A. Jorio, E. H. M. Ferreira, F. Stavale, C. A. Achete, R. B. Capaz, M. V. O. Moutinho, A. Lombardo, T. S. Kulmala and A. C. Ferrari, *Nano Lett.*, 2011, **11**, 3190-3196.
31. B. Guo, Q. Liu, E. Chen, H. Zhu, L. Fang and J. R. Gong, *Nano Lett.*, 2010, **10**, 4975-4980.
32. V. Iberi, L. Liang, A. V. Ievlev, M. G. Stanford, M.-W. Lin, X. Li, M. Mahjouri-Samani, S. Jesse, B. G. Sumpter and S. V. Kalinin, *Sci. Rep.*, 2016, **6**, 30481.
33. D. Teweldebrhan and A. A. Balandin, *App. Phys. Lett.*, 2009, **94**, 013101.
34. H.-P. Komsa, J. Kotakoski, S. Kurasch, O. Lehtinen, U. Kaiser and A. V. Krasheninnikov, *Phys. Rev. Lett.*, 2012, **109**, 035503.
35. W. M. Parkin, A. Balan, L. Liang, P. M. Das, M. Lamparski, C. H. Naylor, J. A. Rodríguez-Manzo, A. T. C. Johnson, V. Meunier and M. Drndić, *ACS Nano*, 2016, **10**, 4134-4142.
36. A. W. Robertson, C. S. Allen, Y. A. Wu, K. He, J. Olivier, J. Neethling, A. I. Kirkland and J. H. Warner, *Nat. Commun.*, 2012, **3**, 1144.
37. W. Li, X. Wang, X. Zhang, S. Zhao, H. Duan and J. Xue, *Sci. Rep.*, 2015, **5**, 9935.
38. P. Ahlberg, F. Johansson, Z.-B. Zhang, U. Jansson, S.-L. Zhang, A. Lindblad and T. Nyberg, *APL Mater.*, 2016, **4**, 046104.
39. Y.-C. Lin, C.-Y. Lin and P.-W. Chiu, *Appl. Phys. Lett.*, 2010, **96**, 133110.
40. M. Chen, H. Nam, S. Wi, G. Priessnitz, I. M. Gunawan and X. Liang, *ACS Nano*, 2014, **8**, 4023-4032.
41. G. Imamura and K. Saiki, *ACS Appl. Mater. Interfaces*, 2015, **7**, 2439-2443.
42. J. J. McMorrow, C. D. Cress, H. N. Arnold, V. K. Sangwan, D. Jariwala, S. W. Schmucker, T. J. Marks and M. C. Hersam, *Appl. Phys. Lett.*, 2017, **110**, 073102.

 This journal is © The Royal Society of Chemistry 2012

View Article Online
DOI: 10.1039/C7NR01712J

43. Z. H. Ni, H. M. Wang, Y. Ma, J. Kasim, Y. H. Wu and Z. X. Shen, *ACS Nano*, 2008, **2**, 1033-1039.
44. S.-M. Kim, Y. Cho, J.-H. Kim, H.-J. Lee, J.-M. Yang and S.-M. Lee, *Nanoscale*, 2014, **6**, 5639-5644.
45. T. Yoon, J.-H. Kim, J. H. Choi, D. Y. Jung, I.-J. Park, S.-Y. Choi, N. S. Cho, J.-I. Lee, Y.-D. Kwon and S. Cho, *ACS Nano*, 2016, **10**, 1539-1545.
46. E. Zion, A. Butenko, Y. Kaganovskii, V. Richter, L. Wolfson, A. Sharoni, E. Kogan, M. Kaveh and I. Shlimak, *J. Appl. Phys.*, 2017, **121**, 114301.
47. J. Chen, T. Shi, T. Cai, T. Xu, L. Sun, X. Wu and D. Yu, *Appl. Phys. Lett.*, 2013, **102**, 103107.
48. S. Bertolazzi, S. Bonacchi, G. Nan, A. Pershin, D. Beljonne and P. Samorì, *Adv. Mater.*, 2017, 1606760-n/a.
49. X. Wang, S. M. Tabakman and H. Dai, *J. Am. Chem. Soc.*, 2008, **130**, 8152-8153.
50. J. M. P. Alaboson, Q. H. Wang, J. D. Emery, A. L. Lipson, M. J. Bedzyk, J. W. Elam, M. J. Pellin and M. C. Hersam, *ACS Nano*, 2011, **5**, 5223-5232.
51. S. Jandhyala, G. Mordi, B. Lee, G. Lee, C. Floresca, P.-R. Cha, J. Ahn, R. M. Wallace, Y. J. Chabal, M. J. Kim, L. Colombo, K. Cho and J. Kim, *ACS Nano*, 2012, **6**, 2722-2730.
52. J. H. Park, S. Fathipour, I. Kwak, K. Sardashti, C. F. Ahles, S. F. Wolf, M. Edmonds, S. Vishwanath, H. G. Xing, S. K. Fullerton-Shirey, A. Seabaugh and A. C. Kummel, *ACS Nano*, 2016, **10**, 6888-6896.
53. H. Liu, K. Xu, X. Zhang and P. D. Ye, *Appl. Phys. Lett.*, 2012, **100**, 152115.
54. A. C. Ferrari, *Solid State Commun.*, 2007, **143**, 47-57.
55. B. Elman, M. Dresselhaus, G. Dresselhaus, E. Maby and H. Mazurek, *Phys. Rev. B*, 1981, **24**, 1027.
56. F. Tuinstra and J. L. Koenig, *J. Chem. Phys.*, 1970, **53**, 1126-1130.
57. A. Eckmann, A. Felten, A. Mishchenko, L. Britnell, R. Krupke, K. S. Novoselov and C. Casiraghi, *Nano Lett.*, 2012, **12**, 3925-3930.
58. S. D. Costa, J. Ek Weis, O. Frank and M. Kalbac, *Carbon*, 2016, **98**, 592-598.
59. G. Compagnini, F. Giannazzo, S. Sonde, V. Raineri and E. Rimini, *Carbon*, 2009, **47**, 3201-3207.
60. A. Felten, B. S. Flavel, L. Britnell, A. Eckmann, P. Louette, J. J. Pireaux, M. Hirtz, R. Krupke and C. Casiraghi, *Small*, 2013, **9**, 631-639.
61. J. Yan, Y. Zhang, P. Kim and A. Pinczuk, *Phys. Rev. Lett.*, 2007, **98**, 166802.
62. S. Mignuzzi, A. J. Pollard, N. Bonini, B. Brennan, I. S. Gilmore, M. A. Pimenta, D. Richards and D. Roy, *Phys. Rev. B*, 2015, **91**, 195411.
63. S. Mouri, Y. Miyauchi and K. Matsuda, *Nano Lett.*, 2013, **13**, 5944-5948.
64. C. Coletti, C. Riedl, D. S. Lee, B. Krauss, L. Patthey, K. von Klitzing, J. H. Smet and U. Starke, *Phys. Rev. B*, 2010, **81**, 235401.
65. B. Radisavljevic and A. Kis, *Nat. Mater.*, 2013, **12**, 815-820.
66. W. Zhu, T. Low, Y. H. Lee, H. Wang, D. B. Farmer, J. Kong, F. Xia and P. Avouris, *Nat. Commun.*, 2014, **5**, 3087.
67. S. Ryu, M. Han, J. Maultzsch, T. Heinz, P. Kim, M. Steigerwald and L. Brus, *Nano Lett.*, 2008, **8**, 4597-4602.

Published on 12 June 2017. Downloaded by University of California - San Diego on 12/06/2017 20:17:49.

Nanoscale Accepted Manuscript

This journal is © The Royal Society of Chemistry 2012